Sensors and Materials, Vol. 31, No. 11 (2019) 3717–3732
MYU Tokyo

S & M 2044

Intersection Point Determination of Parabolic Antenna Reflectors Using Close-range Photogrammetry

Hyukgil Kim[1] and Sungnam Hong[2*]

[1]MAC Development Team, Hyundai MnSOFT,
Hyundai Motor Building, Wonhyoro 74, Seoul 04365, Republic of Korea
[2]Department of Ocean Civil Engineering, Gyeongsang National University,
Engineering Building, Cheondaegukchi 38, Tongyeong 53064, Republic of Korea

(Received April 22, 2019; accepted October 16, 2019)

Keywords: nontarget, close-range photogrammetry, intersection point determination

In the construction of complex antenna structures, a number of feature points are inevitably formed on the main reflector surface of the antenna structure by bolting, riveting, cabling, and welding. In this study, the intersection point determination method using close-range photogrammetry was investigated. 3D position coordinates of many feature points distributed on the inner surface of a parabolic reflector were extracted using close-range photogrammetry. The fitting lines were estimated for the feature points arranged in the radial direction of the parabolic reflector, which tend to intersect at the center point of the reflector. The intersection point between the estimated fitting lines was calculated. The numerical variation of the intersection points on the three axes, which are accumulated through regular time-series calculations, can be used to intuitively predict and analyze not only the deformation rates but also the deformation directions for the shape of the parabolic reflector.

1. Introduction

The measurement techniques used to study the structural behavior of complex structures are classified into traditional contact and noncontact methods. Traditional contact measurement techniques provide limited experimental data for one or two directions at a single point mounted with an instrument.(1) These techniques have limitations in analyzing the overall shape deformation of the structure and are not suitable for measuring the entire surface of the object in which many measuring points are distributed.(2) On the other hand, the noncontact measurement technique provides the opportunity to measure a number of measuring points distributed on the object surface in 3D with reliable accuracy.(3) Accordingly, advanced optical measurement methods should be applied to ensure a wide range of measurements for all the measuring points of the object in order to enhance our understanding of the practical structural behavior of complex structures.

Antenna structures are complex structures with huge weight built with various components and materials. It is very important to identify and understand the structural behaviors of such huge complex structures that are subjected to extreme loads. The structural behaviors

*Corresponding author: e-mail: snhong@gnu.ac.kr
https://doi.org/10.18494/SAM.2019.2415

ISSN 0914-4935

of complex structures subjected to extreme loads are difficult to identify, such as the load path in components with complex geometries, the effect of boundary conditions, and load transfer through contact surfaces.[4] For these reasons, the application of noncontact detection techniques is very valuable in studying the structural behaviors of complex structures.

In this study, the intersection point determination method based on close-range photogrammetry was investigated. The parabolic reflector of the antenna structure has feature points distributed in the radial direction. Estimating the fitting lines using these feature points leads to a tendency to intersect at the center point of the structure. For this, the precise fitting lines for the 3D position coordinates of the feature points were estimated by the total least squares (TLS) method. The intersection point was calculated using the nearest point calculation algorithm between the nonintersecting lines. Close-range photogrammetry based on a nontarget was applied to efficiently calculate the 3D position coordinates of the feature points, which were used to estimate the fitting lines. By tracking the numerical variation of the intersection points on three axes (X, Y, Z), which are accumulated through regular time-series calculations, the antenna owner and operator can intuitively predict and analyze the deformation directions as well as deformation rates of the parabolic reflector.

2. Close-range Photogrammetry

Close-range photogrammetry is an effective tool for replicating objects through 3D digitization and has been adopted for various applications in medicine, entertainment, archaeology, forensics, and engineering. Close-range photogrammetry is also increasingly used for tracking the movement of structures in both the laboratory and the field. It enables a large number of points to be measured in 3D and can be applied in situations that might be impractical for implementing traditional displacement transducers.[5] If precise camera calibration for the application of close-range photogrammetry is carried out in advance, shape deformations such as curvature and deflection, which occur in the main reflector can be measured with high accuracy. The disadvantages of close-range photogrammetry, such as a position accuracy lower than that of laser scanners, can be complemented by analyzing trends in the deflection through long-term continuous measurements.

To efficiently calculate the 3D position coordinates of the feature points, close-range photogrammetry was applied on the basis of the direct linear transformation (DLT) method and the self-calibration bundle adjustment with additional parameters.[6]

Figure 1 shows the overall process for calculating the 3D position coordinates of the object on the object coordinate system using the orientation parameter results of the stereo image. The target that is attempting to calculate the position on the object coordinate system can be represented by a conjugate point in the stereo image. For one conjugate point in the stereo image, two collinearity condition equations that substitute the orientation parameter results of the left image and two collinearity condition equations that substitute the orientation parameter results of the right image are formulated. Accordingly, a total of four collinearity condition equations are formulated for the position coordinates (X, Y, Z) of the object to be solved. The optimal solution of (X, Y, Z) can be calculated using the least squares (LS).

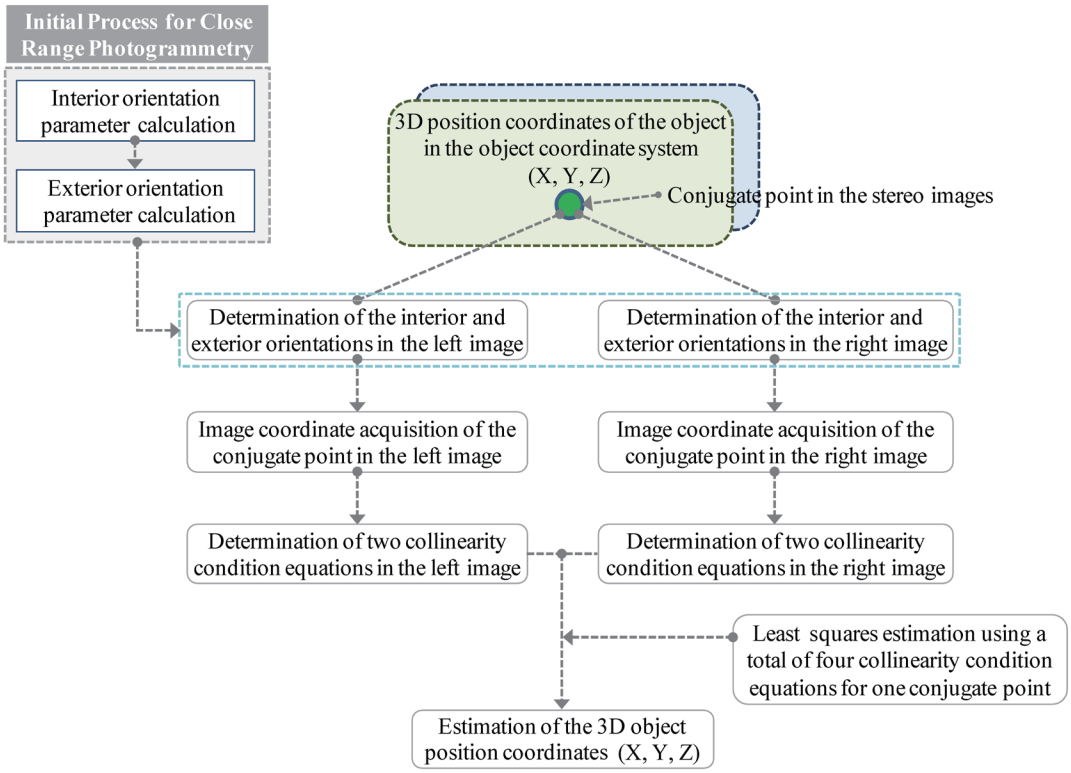

Fig. 1. (Color online) Calculation process for 3D position coordinates of object in the stereo images.

2.1 3D fitting line estimation method

In the field of signal and image processing, adjustment computation through distance calculation has been extensively used as the optimal fitting standard. In particular, various applications have been developed to solve the problems of shape recognition, curve detection, and curve fitting.[7] The optimal fitting standard was presented through orthogonal distance calculation using TLS among various adjustment calculation methods. TLS has been known as the error-in-variables method or the orthogonal linear regression method through various conventional studies and can be represented by Eq. (1). TLS can be specified as the process of calculating the orthogonal distances between measuring points and optimally estimating the fitting line.

$$R = \sum_{i=1}^{n} |d_i|, \tag{1}$$

where R is the correlation coefficient, d is the orthogonal distance, and n is the number of samples.

The actual computation of TLS can be implemented through mathematical methods such as eigenvalue, eigenvector, and principal component analysis (PCA). To precisely estimate the linear coefficients of the 3D fitting line equations for the 3D position coordinates of the feature points, PCA was applied. PCA is a method used in expressing a high-dimensional input vector in a low dimensional form. It is an analytical method that reduces the dimension by linearly projecting the entire data to the axis of several eigen directions so as to include the maximum variance. Decreasing the dimensions of the input vector through PCA preserves information about the data distribution, but has effects such as computational load reduction, noise reduction, and data compression.[8] In the calculation process of PCA, singular value decomposition (SVD) is applied to the data matrix. Assuming that the column mean values of the data matrix $\boldsymbol{X}$ are all zero, the SVD of the matrix $\boldsymbol{X}$ can be expressed as

$$\boldsymbol{X} = \boldsymbol{U}\boldsymbol{D}\boldsymbol{V}^{\mathrm{T}}, \tag{2}$$

where $\boldsymbol{X}$ is an $n \times p$ data matrix, n is the number of observations, p is the number of variables, $\boldsymbol{U}$ is an $n \times p$ matrix, $\boldsymbol{D}$ is a $p \times p$ diagonal matrix with the singular values of $\boldsymbol{X}$ on the diagonal, and $\boldsymbol{V}$ is a $p \times p$ matrix with $\boldsymbol{V}^{\mathrm{T}}\boldsymbol{V} = \boldsymbol{V}\boldsymbol{V}^{\mathrm{T}} = \boldsymbol{U}^{\mathrm{T}}\boldsymbol{U} = I_p$.

In Eq. (2), $\boldsymbol{U}\boldsymbol{D}$ is the principal component, the column of $\boldsymbol{V}$ indicates the loading corresponding to the principal component, and the ith variance of the principal component is equal to $\boldsymbol{D}_{ii}^2 / n$. The linear coefficients of the equations of the 3D fitting line fitted optimally to the feature points were estimated using the loadings calculated from Eq. (2).

2.2 Calculation of the nearest point between nonintersecting lines

The fitting lines estimated using TLS for feature points distributed on the inner surface of the parabolic reflector do not form the intersection point with exactly one solution. Therefore, the calculation result of the nearest point of the nonintersecting fitting lines is used as the fundamental data to determine the shape deformation of the parabolic reflector. To achieve this, the nearest point, which can be defined as the intersection point of the fitting lines, was calculated using the intersection point calculation algorithm between the nonintersecting lines. The intersection point calculation algorithm of nonintersecting lines used in this study is described as follows.[9–13]

In the case of two dimensions, the point on the ith line is represented by p_i, and the unit normal vector, which is perpendicular to the ith line, is represented by $\hat{\boldsymbol{n}}_i$. If x_1 and x_2 are random points located on the first line, $p_1 = x_1$ can be set, and the unit vector $\hat{\boldsymbol{n}}_i$ rotated vertically to the line can be represented as

$$\hat{\boldsymbol{n}}_1 \triangleq \begin{bmatrix} 0 & -1 \\ 1 & 0 \end{bmatrix} (x_2 - x_1) / \left\| x_2 - x_1 \right\|, \tag{3}$$

where x_1 and x_2 are points on the first line, and $\hat{\boldsymbol{n}}_i$ is the unit normal vector.

The distance from the random point x to a point on the line represented by $(p, \hat{n})$ can be expressed as Eq. (4), and the squared distance can be expressed as

$$d\left(x,(p,n)\right)=\left\|(x-p)\,\hat{\boldsymbol{n}}\right\|=\left\|(x-p)^{\mathrm{T}}\,\hat{\boldsymbol{n}}\right\|=\sqrt{(x-p)^{\mathrm{T}}\,\hat{\boldsymbol{n}}\hat{\boldsymbol{n}}^{\mathrm{T}}(x-p)}, \tag{4}$$

where $d(x, (p, n))$ is the distance from a point x to the line $(p, \hat{n})$.

$$d\left(x,(p,n)\right)^2=(x-p)^{\mathrm{T}}\left(\hat{\boldsymbol{n}}\hat{\boldsymbol{n}}^{\mathrm{T}}\right)(x-p) \tag{5}$$

Here, $d(x, (p, n))^2$ is the squared distance from a point x to the line $(p, \hat{n})$.

The sum of the squared distances for a number of lines represented in 2D can be expressed as Eq. (6) as a cost function. Equation (6) can be expanded and aligned as Eq. (7).

$$E(x)=\sum_i(x-p_i)^{\mathrm{T}}\left(\hat{\boldsymbol{n}}_i\hat{\boldsymbol{n}}_i^{\mathrm{T}}\right)(x-p_i) \tag{6}$$

$$\begin{aligned}E(x)&=\sum_i x^{\mathrm{T}}\hat{\boldsymbol{n}}_i\hat{\boldsymbol{n}}_i^{\mathrm{T}}x-x^{\mathrm{T}}\hat{\boldsymbol{n}}_i\hat{\boldsymbol{n}}_i^{\mathrm{T}}x-p_i^{\mathrm{T}}\hat{\boldsymbol{n}}_i\hat{\boldsymbol{n}}_i^{\mathrm{T}}x\\&=x^{\mathrm{T}}\left(\sum_i\hat{\boldsymbol{n}}_i\hat{\boldsymbol{n}}_i^{\mathrm{T}}\right)x-2x^{\mathrm{T}}\left(\sum_i\hat{\boldsymbol{n}}_i\hat{\boldsymbol{n}}_i^{\mathrm{T}}p_i\right)-2x^{\mathrm{T}}\left(\sum_i\hat{\boldsymbol{n}}_i\hat{\boldsymbol{n}}_i^{\mathrm{T}}p_i\right)\end{aligned} \tag{7}$$

Here, $E(x)$ is the sum of the squared distances to many lines.

Under the condition that the result of the differentiation of Eq. (7) with respect to x is equal to zero vector, the minimum value x can be calculated as described in Eq. (8). The minimum value x indicates the nearest point between the lines that do not intersect in 2D.

$$\begin{aligned}\frac{\partial E(x)}{\partial x}=\mathbf{0}&=2\left(\sum_i\hat{\boldsymbol{n}}_i\hat{\boldsymbol{n}}_i^{\mathrm{T}}\right)x-2\left(\sum_i\hat{\boldsymbol{n}}_i\hat{\boldsymbol{n}}_i^{\mathrm{T}}p_i\right)\\\left(\sum_i\hat{\boldsymbol{n}}_i\hat{\boldsymbol{n}}_i^{\mathrm{T}}\right)x&=\sum_i\hat{\boldsymbol{n}}_i\hat{\boldsymbol{n}}_i^{\mathrm{T}}p_i\\x&=\left(\sum_i\hat{\boldsymbol{n}}_i\hat{\boldsymbol{n}}_i^{\mathrm{T}}\right)^{-1}\left(\sum_i\hat{\boldsymbol{n}}_i\hat{\boldsymbol{n}}_i^{\mathrm{T}}p_i\right)\end{aligned} \tag{8}$$

Here, x is the nearest point to the nonintersecting lines in 2D.

In the case of more than three dimensions, the nearest point x between the nonintersecting lines is calculated as follows. $\hat{\boldsymbol{n}}_i$ can be generalized to any number of dimensions by noting

that $\hat{\boldsymbol{n}}_i\hat{\boldsymbol{n}}_i^{\mathrm{T}}$ is simply the (symmetric) matrix with all eigenvalues being unity except for zero eigenvalue in the direction along the line providing a seminorm on the distance between p_i and another point giving the distance to the line. In any number of dimensions, if $\hat{\boldsymbol{v}}_i$ is a unit vector along the ith line, $\hat{\boldsymbol{n}}_i\hat{\boldsymbol{n}}_i^{\mathrm{T}}$ can be defined as $\boldsymbol{I}-\hat{\boldsymbol{v}}_i\hat{\boldsymbol{v}}_i^{\mathrm{T}}$. As a result, the nearest point x to nonintersecting lines in 3D can be expressed as

$$x=\left(\sum_i \boldsymbol{I}-\hat{\boldsymbol{v}}_i\hat{\boldsymbol{v}}_i^{\mathrm{T}}\right)^{-1}\left(\sum_i\left(\boldsymbol{I}-\hat{\boldsymbol{v}}_i\hat{\boldsymbol{v}}_i^{\mathrm{T}}\right)p_i\right), \tag{9}$$

where x is the nearest point to the nonintersecting lines in 3D, $\boldsymbol{I}$ is the identity matrix, and $\hat{\boldsymbol{v}}_i$ is a unit vector along the ith line.

3. Experiment Program

3.1 Target structure

The parabolic reflector of a very long baseline interferometer (VLBI) antenna was selected as the target structure. The VLBI antenna is located at the Space Geodetic Observation Center (SGOC) in South Korea and consists of a main parabolic reflector with a diameter of 22 m and a subreflector with a diameter of 2.2 m. The general specifications of the VLBI antenna structure are presented in Table 1.

3.2 Experiment configuration for close-range photogrammetry

To carry out close-range photogrammetry successfully, various types of targets should be configured on the subject, and an accurate measurement process for each target should be carried out. The target configuration can be classified into the application of feature points that

Table 1
Specifications of the VLBI antenna structure used in the study.

Classification	Explanation
Antenna diameter	Parabolic reflector: 22 m, Subreflector: 2.2 m
Antenna type	Cassegrain dual reflector and FSS reflector for band selector
Reflector	Shaping formed aluminum panels, welded steel back-up structure frequency selective mirror
Pedestal configuration	Elevation over azimuth pedestal, made of steel yoke tower
Azimuth travel	±270°
Elevation travel	0–90°
Azimuth travel rate	> 5°/s
Elevation travel rate	> 5°/s
Receiving frequency band	2, 8, 22, and 43 GHz
Antenna illumination efficiency	−60%
Precision of antenna pointing	0.0131° (RMS)
Precision of parabolic reflector curved surface	86 μm
Foundation (L × W × D)	Base: W15000 × W15000 × 2000H, Yoke: 7000 × 4700H

are distinguished from other pixels in the captured image of the subject, or the attachment of reflective targets that are suitably produced. When the feature points located on the structure surface are used as targets, close-range photogrammetry has the advantage of carrying out noncontact detection without attaching reflective targets to structures that are likely to be deformed.

A large-scale reflector has been manufactured according to a standardized construction method as a circular structure assembled by arranging hundreds of metal panels. In the construction process of joining and fixing each metal panel to build the main reflector, many feature points are inevitably formed on the main reflector surface by bolting, riveting, cabling, and welding. Thus, the accuracy of close-range photogrammetry can be maintained by replacing reflective targets with many feature points distinguished from other pixels in the image.

The parabolic reflector of the VLBI antenna with a diameter of 22 m is suitable for applying nontarget based close-range photogrammetry because many feature points are distributed on the structure surface. A total of 210 feature points distributed on the inner surface of the parabolic reflector were used as target points for the application of nontarget based close-range photogrammetry. To match the image coordinates of the feature points on the VLBI antenna surface with the results of the ground control point coordinates, a total of 210 feature points were labeled, as shown in Fig. 2. Then, the labeled feature points that are easily distinguishable with the naked eye were selected. Because the selected feature points were evenly distributed on the reflector surface, the parabolic shape of the reflector could be accurately perceived.

Figure 3 shows the stereo images of the parabolic reflector taken by two nonmetric cameras. To obtain the stereo images, Arecont Vision model AV10005DN cameras (Los Angeles, CA, USA) were used, which can measure 10-megapixel images at 6 FPS. The details and measurement procedure for the feature points, including two cameras and a total station, were described by the authors.[(2)]

To calculate the precise interior and exterior orientation parameters of nonmetric cameras, the image coordinates for a total of feature points were obtained, and a control point survey was conducted using the total station. The control point coordinates measured using the total

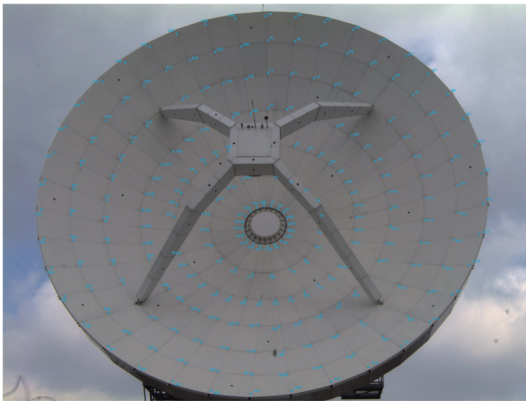

Fig. 2. (Color online) Feature points distributed on the inner surface of the parabolic reflector labeled to match the measurement results of image and control point coordinates.

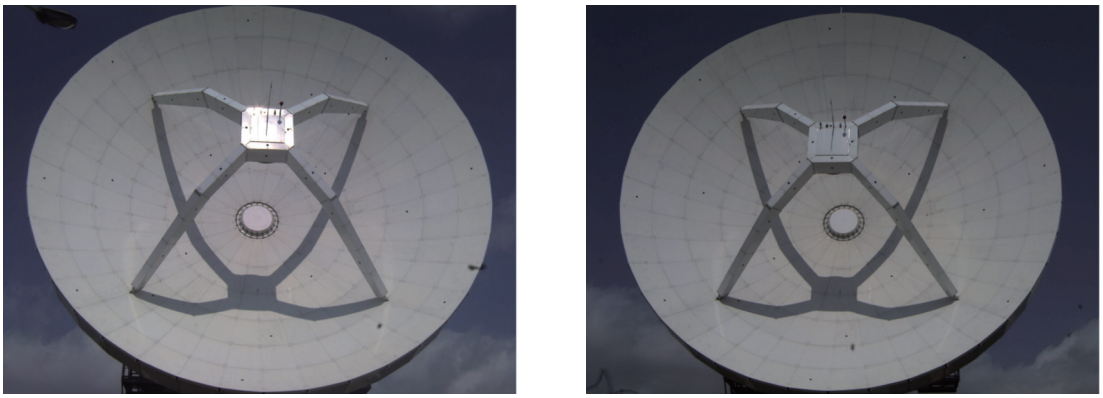

(a) (b)

Fig. 3. (Color online) Stereo images of the parabolic reflector of VLBI antenna taken by two nonmetric cameras: (a) first and (b) second images.

station were used as the reference coordinates for the calculation of the camera calibration and orientation parameters. When the 3D position coordinates of the feature points were recalculated using the calculation results of the precise interior and exterior orientation parameters, the control point coordinates were used as the reference coordinates for evaluating the accuracy of the recalculated position coordinates. An S8 total station from Trimble was used to carry out the ground control point survey. The nontarget measurement using the total station showed accuracy and error ranges of ± (2 mm + 2 ppm × D) in the standard mode and ± (4 mm + 2 ppm × D) in the tracking mode.

The interior and exterior orientation parameters were calculated using the image and control point coordinates of the 210 feature points acquired in the above process, respectively. To analyze the position accuracy of the close-range photogrammetry, the same 210 feature points in the stereo image were all selected as the conjugate points, and their 3D position coordinates were calculated. The conjugate points are the same points in the stereo images and the object of the 3D coordinate calculation after obtaining the orientation results. The accuracy analysis of close-range photogrammetry was carried out by comparing the 3D position coordinates calculated using the conjugate points of the stereo images with the reference coordinates for the same points measured by the total station survey.

3.3 Estimation plan for 3D fitting lines and intersection point

According to the estimation plan for the fitting lines and intersection points for carrying out noncontact detection for the shape deformation of the parabolic reflector, 128 feature points out of a total of 210 were selected as the fitting target points. Figure 4 shows the 3D position coordinate distribution of the selected feature points calculated using close-range photogrammetry for the fitting line estimation from the many feature points located on the inner surface of the parabolic reflector. The intersection points between the entire fitting lines, which are expressed as equations of straight lines in 3D, were then calculated. The fitting line estimation is based on a premise that the feature points located at the center of the parabolic

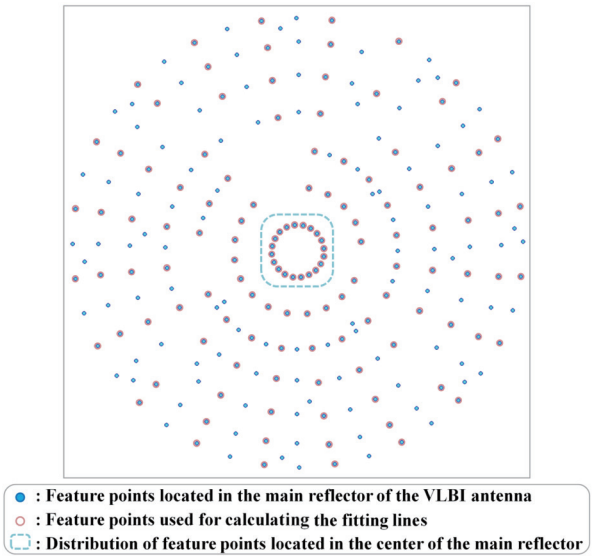

Fig. 4. (Color online) Distribution of the feature points located in the parabolic reflector used for calculating the fitting lines.

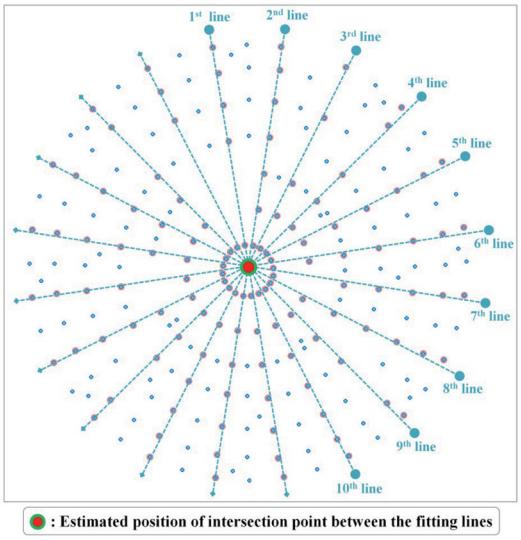

Fig. 5. (Color online) Calculation plans for the estimation of fitting lines and the position of the intersection point.

reflector must be included. This is because the intersection point of the entire fitting lines is expected to be located within the distribution range of the feature points located at the center of the parabolic reflector.

Figure 5 shows the estimation schemes for a total of 10 fitting lines calculated for 128 feature points distributed on the straight lines based on the centrally located feature points and the intersection points calculated using the estimated fitting lines. The fitting line estimation was planned in all directions of the parabolic reflector surface so that the entire shape of the parabolic reflector can be expressed. The intersection point of the estimated 10 fitting lines was used as intuitive basic data, which can judge the shape deformation possibility of the parabolic reflector.

4. Research Results

4.1 Accuracy analysis of close-range photogrammetry

To apply the nonmetric camera to close-range photogrammetry, the process of calculating the precise interior and exterior orientation parameters of the camera should be explained. The initial values for bundle adjustment were calculated by applying the DLT method using the coordinates from the stereo images and the ground control point survey results. To calculate the 3D position coordinates of a total of 210 conjugate points, the precise interior and exterior orientation parameters of the stereo images were finally determined through self-calibration bundle adjustment with additional parameters using the initial orientation results calculated by the DLT method. After linearizing the nonlinear collinearity equation through the Taylor series, the Jacobian and observation matrices were constructed to implement bundle adjustment. The

final convergence values of the interior and exterior orientations were calculated by iteratively calculating the orientation parameters using LS.

The results of the exterior orientation parameters among the camera orientation parameters calculated using bundle adjustment are presented in Table 2, and the results of the interior orientation parameters are presented in Table 3. Omega, Phi, and Kappa are the camera orientation angles, and X_L, Y_L, and Z_L are the positions of the perspective center in Table 2. x_0 and y_0 are the coordinates of the principal point, K_1, K_2, and K_3 are the radial distortion coefficients, and P_1 and P_2 are the tangential distortion coefficients in Table 3.

To analyze the accuracy of the nontarget based close-range photogrammetry, the 3D position coordinates of 210 conjugate points distributed on the inner surface of the parabolic reflector were calculated. For this purpose, LS estimation for the 3D position coordinates was implemented by substituting the image coordinates for the conjugate points of the stereo image and the interior and exterior orientation parameters that were calculated with bundle adjustment in the collinearity equation.

The statistical analysis of the deviation between the 3D position coordinates of the 210 conjugate points and the total station measurements of the same points used as the check points was carried out to determine the accuracy of the close-range photogrammetry, as presented in Table 4. The 3D position coordinates of the conjugate points were $X = 0.078 \pm 3.827$ mm, $Y = -0.174 \pm 3.684$ mm, and $Z = 0.197 \pm 3.719$ mm in the *X*-, *Y*-, and *Z*-axis directions, respectively. The maximum deviations for each axis were calculated as 8.856, 8.852, and 8.877 mm in the *X*-, *Y*-, and *Z*-axis directions, respectively. As a result, the 3D shape of the parabolic reflector was precisely identified using the 3D position coordinates calculated with millimeter-level accuracy through nontarget-based close-range photogrammetry.

Table 2
Results of exterior orientation parameters calculated using bundle adjustment in the parabolic reflector.

Images	Omega (rad)	Phi (rad)	Kappa (rad)	X_L (*m*)	Y_L (*m*)	Z_L (*m*)
First image	3.2821	−1.1469	1.6260	−0.2513	16.6135	−0.6715
Second image	2.3751	−1.0263	0.7272	1.3904	0.0520	−0.7458

Table 3
Results of interior orientation parameters calculated using bundle adjustment in the parabolic reflector.

Images	x_0 (pixel)	y_0 (pixel)	K_1 (mm^{-2})	K_2 (mm^{-4})	K_3 (mm^{-6})	P_1 (mm^{-1})	P_2 (mm^{-1})	Pixel size (width)	Pixel size (height)
First image	705.1929	−315.9368	2.8078 E−08	3.7221 E−16	8.8529 E−23	3.5629 E−07	3.1287 E−07	2592	1944
Second image	682.2845	−335.8074	2.2597 E−08	1.1757 E−15	−8.7920 E−23	−1.8908 E−08	3.1096 E−07	2592	1944

Table 4
Statistical indicators of the deviations between the 3D position coordinates of the conjugate points and the total station measurements in the parabolic reflector.

Statistical indicator	*X*-axis coordinates (mm)	*Y*-axis coordinates (mm)	*Z*-axis coordinates (mm)
Maximum deviation	8.675	7.758	8.861
Minimum deviation	−8.856	−8.852	−8.877
Average deviation	0.078	−0.174	0.197
Standard deviation	3.827	3.684	3.719

4.2 Fitting line estimation results

Figure 6 shows the 3D position coordinates of the feature points to be estimated for the fitting lines. The overall distribution of the feature points located on the inner surface of the parabolic reflector was expressed. Close-range photogrammetry based on a nontarget using DLT and bundle adjustment was used to calculate the 3D position coordinates for a total of 128 feature points.

The reason for the discontinuity, which resulted in feature points that do not exist at the points where each fitting line is expected to be estimated in Fig. 6, is as follows. The feature points that are difficult to observe owing to the front structure of the parabolic reflector at the time of the total station survey and image acquisition were excluded from the fitting objects because the control point survey and image coordinate measurement for these points are impossible.

Figure 7(a) shows the distribution of the feature points for the estimation of the first fitting line, while Fig. 7(b) shows the result of the first fitting line estimated using TLS for the feature points distributed in 3D space and the equation of the corresponding fitting line. In Fig. 7(a), 3D position coordinates for each feature point calculated through close-range photogrammetry based on a nontarget were expressed using circles. In Fig. 7(b), the fitting line estimated by applying TLS to the position coordinates of the feature points and the orthogonal distance between each feature point and the fitting line are shown.

Figures 8(a) and 8(b) illustrate the tendency that more than two fitting lines estimated using TLS intersect in 3D space. The feature points to be fitted are distributed in certain directions on the inner surface of the parabolic reflector. When the fitting lines are estimated for feature points located along each direction, a tendency to intersect at the center of the parabolic

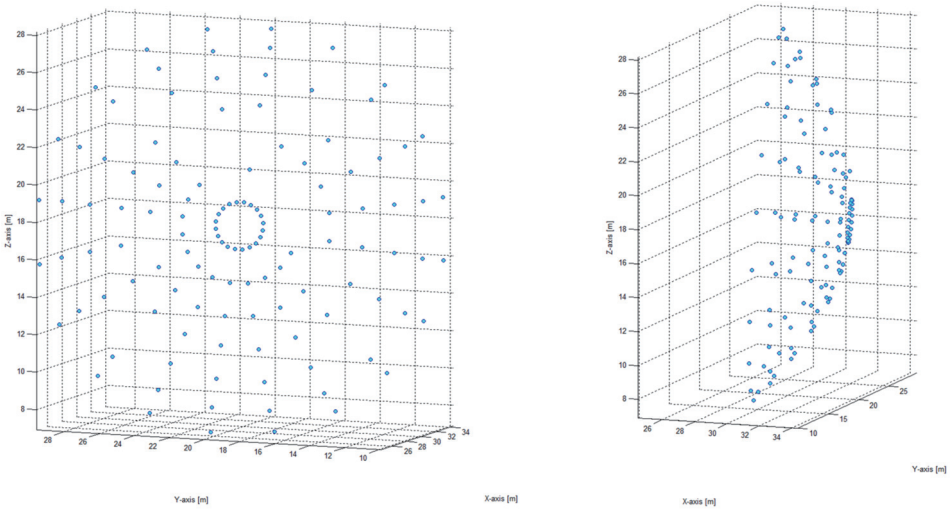

(a) (b)

Fig. 6. (Color online) 3D position coordinates of the feature points located in the inner surface of the parabolic reflector: (a) front and (b) side of the parabolic reflector.

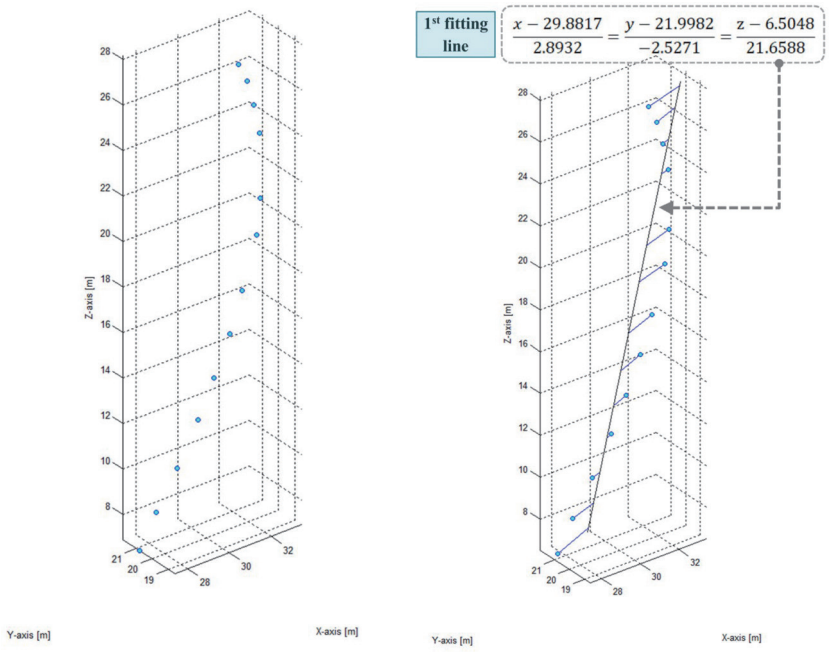

Fig. 7. (Color online) Estimation results of the fitting line in 3D space using TLS for shape deformation detection: (a) distribution of the feature points for the estimation of the first fitting line and (b) determination of the first fitting line in 3D space using TLS.

reflector occurs, as shown in Fig. 8(c). In addition, Fig. 8(c) shows that the 3D fitting lines estimated for the feature points do not form the intersection point with exactly one solution.

4.3 Intersection point calculation results

Figure 9 shows ten fitting lines estimated for a total of 128 feature points distributed on the inner surface of the parabolic reflector. The intersection point calculated for the fitting lines represented by the equation of straight lines in 3D space was used as the fundamental data for the noncontact detection of shape deformation occurring in parabolic structures such as the parabolic reflector. However, the 10 fitting lines estimated from the feature points do not have the intersection point with exactly one solution. Therefore, to estimate the intersection point for nonintersecting fitting lines, the nearest point between nonintersecting lines represented by the equation of straight lines in 3D space was calculated.

Figure 10 shows the result of the nearest point calculated using the above process. The calculation results of the nearest point were 31.2997, 20.7322, and 17.2993 m.

To evaluate the calculation accuracy of the fitting lines estimated through TLS, the deviations between the 3D position coordinates of the 128 feature points to be fitted and the 3D position coordinates of the specific points on the fitting lines that are orthogonal to each feature point were calculated. Table 5 shows the results of the statistical analysis of the calculated deviations. Each mean value of the deviations calculated for the three axes converged to zero,

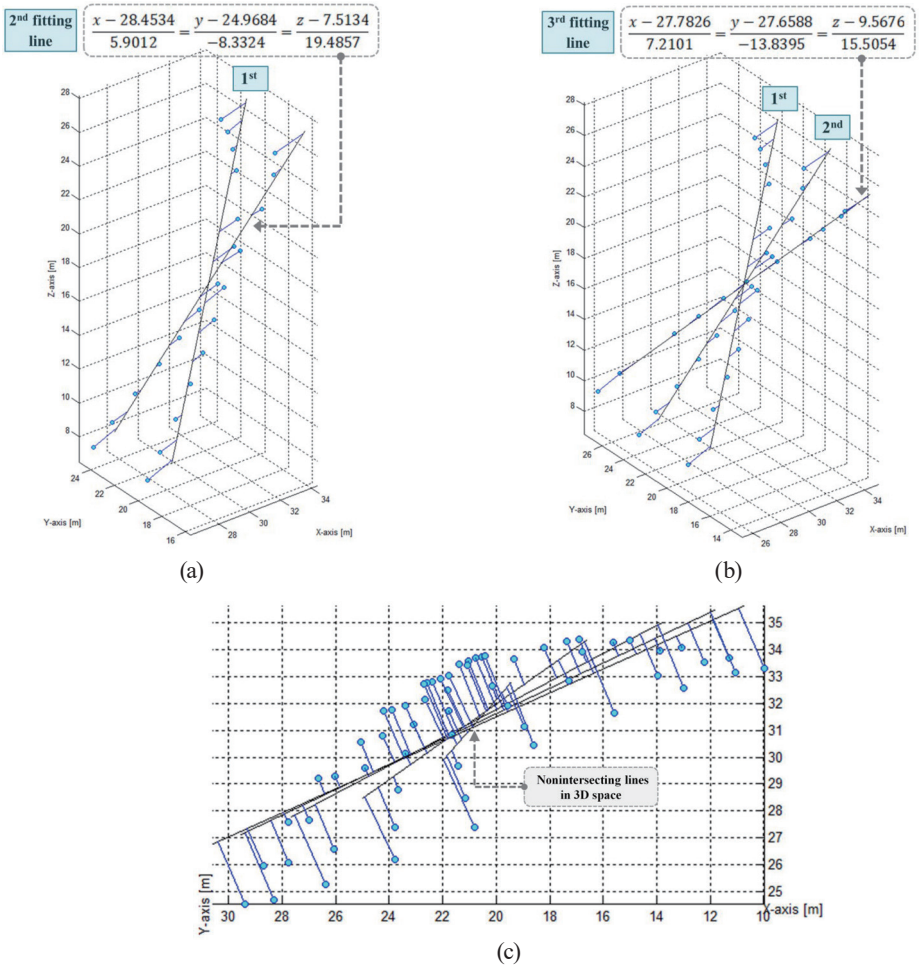

Fig. 8. (Color online) Intersection tendencies of the estimated fitting lines in 3D space: (a) second fitting line, (b) third fitting line, and (c) nonintersecting lines in 3D space.

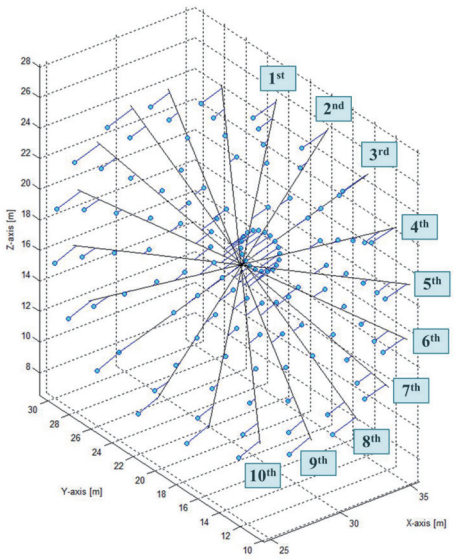

Fig. 9. (Color online) Estimation of 10 fitting lines for shape deformation detection of the parabolic reflector.

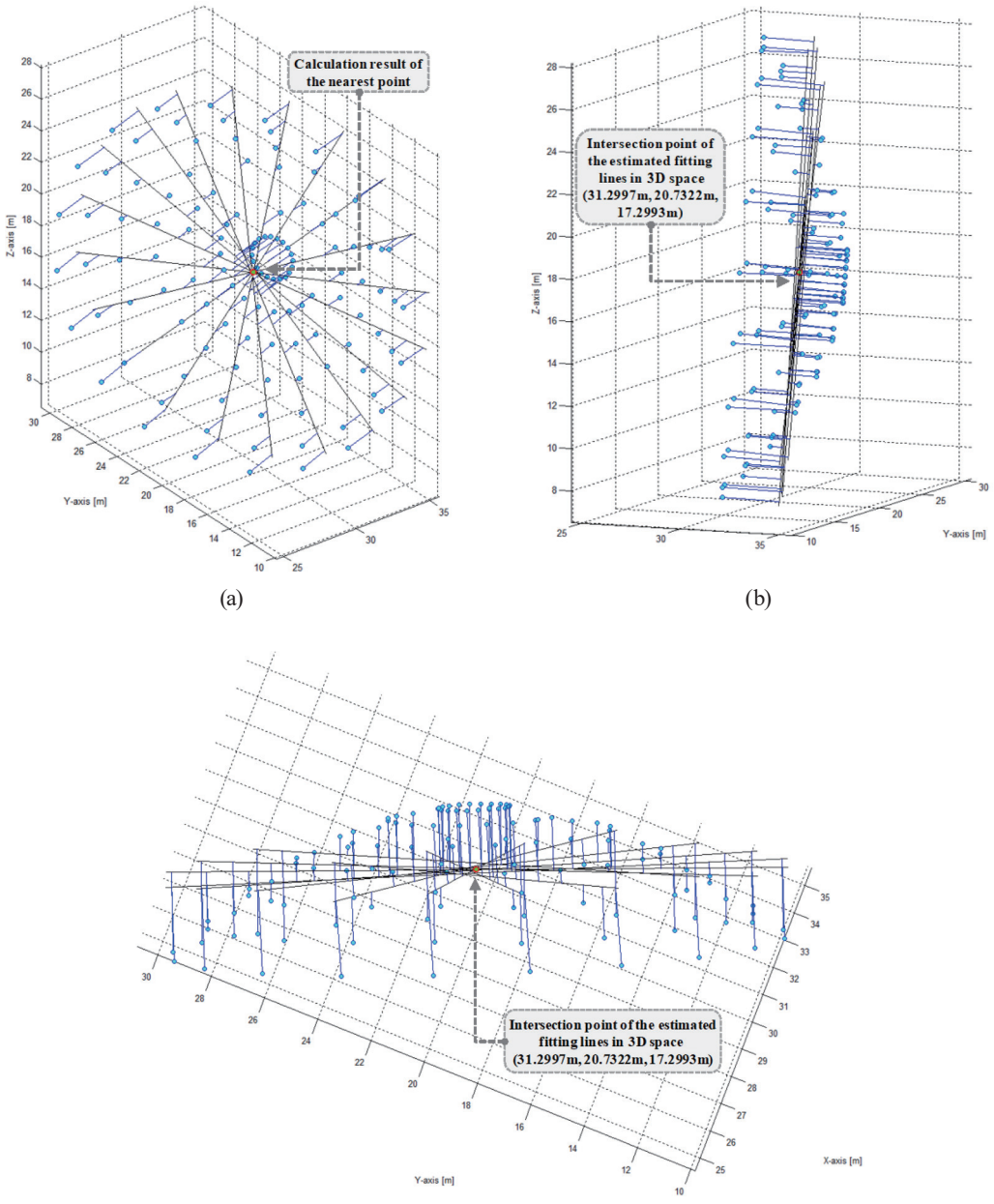

Fig. 10. (Color online) Intersection point determined by the calculation of the nearest point to nonintersecting lines: (a) calculation result of the nearest point, (b) intersection point of the estimated fitting lines in 3D space (side view), and (c) intersection point of the estimated fitting lines in 3D space (aerial view).

Table 5
Statistical indicators of the deviations between the feature points and the estimated fitting lines.

Statistical indicator	*X*-axis coordinates (m)	*Y*-axis coordinates (m)	*Z*-axis coordinates (m)
Maximum deviation	2.656	1.181	0.245
Minimum deviation	−2.183	−0.972	−0.327
Average deviation	0.000	0.000	0.000
Standard deviation	1.558	0.674	0.147

as indicated in Table 5. These results indicate that the fitting lines can be estimated by TLS along the appropriate paths where the deviations are minimized.

5. Conclusions

In this study, the intersection point determination method using nontarget based close-range photogrammetry was applied to detect the shape deformation of complex structures with intricate geometries. To achieve this, the intersection point determination method was embodied in the following process. The 3D position coordinates of feature points selected for the estimation of fitting lines were calculated using nontarget based close-range photogrammetry. A total of 10 fitting lines were estimated in all directions of the parabolic reflector surface so that the overall shape of the parabolic reflector can be expressed using the 3D position coordinates of the calculated feature points. To optimally fit feature points distributed in 3D into the equations of straight lines, the linear coefficients of the equations for the 3D fitting lines were precisely estimated by the TLS method based on PCA.

The feature points to be fitted were uniformly distributed in the radial direction on the inner surface of the parabolic reflector. The 10 fitting lines estimated from these feature points do not form the intersection point with exactly one solution. Thus, the nearest point, which can be defined as the intersection point of these 10 fitting lines, was calculated using the intersection point calculation algorithm between the nonintersecting lines. The calculation results of the nearest point were 31.2997, 20.7322, and 17.2993 m. The numerical variations of the intersection points in the 3 axes accumulated through periodic time-series calculations can be used as fundamental data that can predict deformation rates as well as deformation directions for the shape of the parabolic reflector. The errors affecting the antenna observation data are expected to be corrected in the future through the time-series analysis of the shape deformation due to the long-term behavior of the antenna structure and the external environment.

Acknowledgments

This work was supported by the Development Fund Foundation, Gyeongsang National University, 2019.

References

1 K. De Wilder, G. De Roeck, and L. Vandewalle: Int. J. Concr. Struct. Mater. **10** (2016) 189. https://doi.org/10.1007/s40069-016-0135-x
2 H. Kim, H. Yun, J. Hwang, and S. Hong: Appl. Sci. **7** (2017) 1125. https://doi.org/10.3390/app7111125
3 L. Taşçi: Exp. Tech. **39** (2015) 3. https://doi.org/10.1111/ext.12022
4 B. Gencturk, K. Hossain, A. Kapadia, E. Labib, and Y. L. Mo: Measurement **47** (2014) 505. https://doi.org/10.1016/j.measurement.2013.09.018
5 A. C. Lovisa, D. J. Henderson, and J. D. Ginger: Exp. Mech. **55** (2015) 599. https://doi.org/10.1007/s11340-014-9977-9
6 E. Mikhail, J. Bethel, and J. McGlone: Introduction to Modern Photogrammetry (Wiley, New York, 2001) p. 78.
7 A. Gruen and D. Akca: ISPRS-J. Photogramm. Remote Sens. **59** (2005) 151. https://doi.org/10.1016/j.isprsjprs.2005.02.006

8 I. T. Jolliffe: Principal Component Analysis (Springer-Verlag, New York, 2002) p. 152.
9 M. De Berg, O. Cheong, M. Van Kreveld, and M. Overmars: Computational Geometry-Algorithms and Applications (Springer-Verlag, New York, 2008) p. 121.
10 J. L. Bentley and T. A. Ottmann: IEEE Trans. Comput. C-**28** (1979) 643. https://doi.org/ 10.1109/TC.1979.1675432
11 R. Goldman and A. S. Glassner: Intersection of Two Lines in Three-Space, ed. A. S. Glassner (Academic Press Professional, San Diego, 1990) p. 304.
12 F. Antonio: Faster Line Segment Intersection, ed. D. Kirk, and A. S. Glassner (Academic Press Professional, San Diego, 1992) pp. 199.
13 T. Cormen, C. Leiserson, R. Rivest, and C. Stein: Determining Whether Any Pair of Segments Intersects, ed. T. Cormen, C. Leiserson, R. Rivest, and C. Stein (MIT Press, Cambridge, 2001) p. 934.